Applied Mathematical Modelling 79 (2020) 672–684

Contents lists available at ScienceDirect

Applied Mathematical Modelling

journal homepage: www.elsevier.com/locate/apm

Summarizing an Eulerian–Lagrangian model for subsea gas release and comparing release of CO_2 with CH_4*

Jan Erik Olsen*, Paal Skjetne

SINTEF Industry, Postboks 4760 NO-7465 Trondheim, Torgarden, Norway

ARTICLE INFO

Article history:
Received 12 June 2019
Revised 13 October 2019
Accepted 23 October 2019
Available online 31 October 2019

Keywords:
CFD
Mathematical modeling
Subsea gas release
Safety

ABSTRACT

A subsea gas release is a concern for both safety and environment. This can be assessed by mathematical models. The development of an Eulerian–Lagrangian modelling concept to study subsea gas release has taken place over many years and the piecewise enhancements have been documented in the open literature. The model in its current state is summarized in this article. Model simulations are shown to be consistent with different experiments varying in depth from 7 to 138 m. The model can be applied to estimate how gas surfaces into the atmosphere from a subsea source. This is vital input to risk assessments. Due to recent interest in subsea CO_2 storage and transport, a comparison of CO_2- and CH_4-releases has been performed. Model results show that a much smaller fraction of released CO_2 reaches the atmosphere than CH_4 due to the high solubility of CO_2 in water.

1. Introduction

Human life, assets and the environment are at risk during subsea gas releases. The main causes of risks are fire and explosions due to surfacing of hazardous gases, capsizing of rigs and ships due to hydrodynamic loads and pollution of ocean waters. Accidental subsea gas release is normally caused by pipeline failure or drilling operations. Numerous incidents happen annually and historically many of these have resulted in loss of life [1]. These incidents primarily involve natural gas or methane. With the recent interest in carbon storage there is a growing risk of subsea release of CO_2 related to asphyxiation. In order to prevent incidents and apply proper intervention if an incident occurs, a reliable risk assessment is a prerequisite for both natural gas and CO_2 releases.

A risk assessment includes several stages. One of these is estimating how the gas bubbles are dispersed in the ocean and distributed at the surface if they survive all the way to the surface. The predicted surface flux can then be used as input to atmospheric dispersion calculations. Here we only consider the plume in the ocean. Historically this has been studied by so-called *integral models* assuming certain profiles (e.g. Gaussian) for the velocity and bubble volume fraction in the plume [2-6]. Such estimates can also be performed by transient multidimensional CFD modelling of large-scale bubble plumes. With the emergence of affordable computers, solving the full set of the Navier Stoke's equations became possible. CFD modelling of bubble plumes dates back to the 1980's when Schwarz and Turner [7] developed an Eulerian-Eulerian

* This article belongs to the Special Issue: CFD2018 Melbourne.

* Corresponding author.
E-mail addresses: jan.e.olsen@sintef.no, dr.jan.erik.olsen@gmail.com (J.E. Olsen).

https://doi.org/10.1016/j.apm.2019.10.057
0307-904X/

model and Johansen and Boysan [8] developed an axisymmetric Eulerian-Lagrangian model for bubble plumes in bubbly reactors. Bubble plumes in the ocean differ from reactors by their much larger scale. This was addressed by Swan and Moros [9] who applied the axisymmetric Eulerian-Lagrangian concept to subsea gas releases. They were able to account for the large number of bubbles in subsea gas releases by tracking groups of bubbles instead of all individual bubbles. Buscaglia et al. [10] used the Eulerian-Eulerian approach in a full 3D simulation for a 77 m deep release with a moderate release rate.

For more intense release rates which can be observed in incidental release from ruptured pipelines or well blowouts, CFD modelling with the Eulerian–Eulerian approach failed to provide reasonable results [11]. For intense releases the gas is released as a jet. The Eulerian–Eulerian method requires a grid resolution smaller than the release diameter to break up the incoming jet into a dispersed flow. Combined with the need for a very large computational domain covering the entire water column, this is not feasible due to the high computational cost. Thus, a transient full 3D Eulerian–Lagrangian model was recommended by Cloete et al. [11]. It is already a dispersed gas flow by definition (i.e. bubbly flow) as it enters the domain. This marked a shift in technology where full 3D transient CFD based on the Navier-Stokes equations became an alternative to the integral models historically applied to these studies. The modelling concept described in the following sections is the result of further development of the work of Cloete et al. [11] partly published before [12-14]. This article serves as a summary of this research with a full description of the most recent version of the modelling concept including a larger set of validation cases. A new study comparing release behavior of CO_2 and CH_4 is presented. The Eulerian–Lagrangian modelling concept has more recently also been applied to subsea gas release by others, including work by Fraga et al [15]. and Li et al. [16].

2. CFD model

An Eulerian–Lagrangian modelling concept has been chosen to study the large scale bubble plumes emanating from subsea gas releases. The transport of mass, momentum and energy in the ocean (liquid) and atmosphere (gas) is solved in an Eulerian frame of reference by the Navier–Stoke's equations. The location of the sea surface is tracked as an interface between liquid and gas. The bubble motion is calculated in a Lagrangian frame of reference with Newton's second law. Bubble and water motion are strongly coupled through drag and turbulence. The equations defining the modelling concept is described in the following sections.

2.1. Flow dynamics

The flow of bubble plumes is driven by the buoyancy provided by the density difference between the gas bubbles and the surrounding water. As the bubbles rises the drag force transfers momentum between bubbles and surrounding water. This accelerates the water in an upward motion. The water moving upwards is replaced by water which is entrained into the plume horizontally. This entrainment and turbulence spread the bubble plume and gives it a shape of a cone. Since the bubbles are driving the plume dynamics, the bubble motion is described first.

Groups of bubbles known as parcels are tracked throughout the calculations. All bubbles in a parcel share the same properties (e.g. bubble size, density and viscosity). It is sum of all the bubbles in a parcel which defines the source for interactions with the continuous Eulerian field. By tracking the bubbles as parcels instead of individual bubbles, the computational cost of modelling billions of bubbles in a Lagrangian reference frame becomes acceptable. A force balance based on Newton's second law gives the bubble acceleration as

$$\frac{d\boldsymbol{u}_b}{dt} = \frac{\boldsymbol{g}(\rho_b - \rho)}{\rho_b} + \boldsymbol{F}_D + \boldsymbol{F}_{VM} \tag{1}$$

if we account for buoyancy (first term on the right-hand side), drag (second term) and virtual mass (last term). Here t is time, $\boldsymbol{u}_b$ is bubble velocity, $\boldsymbol{g}$ is the gravitational acceleration, ρ_b is the density of the bubble gas and ρ is the density of the sea water (or continuous phase). We use specific forces, i.e. force divided by mass. The specific drag force is

$$\boldsymbol{F}_D = \frac{18\mu}{\rho_b d_b^2}\frac{C_D \mathrm{Re}}{24}(\boldsymbol{u} - \boldsymbol{u}_b) \tag{2}$$

where Re is the Reynolds number, C_D is the drag coefficient, and d_b is the bubble diameter. The drag coefficient is provided by the expression of Tomiyama et al. [17] for partly contaminated conditions

$$C_{D0} = \max\left\{\min\left[\frac{24}{\mathrm{Re}}\left(1 + 0.15\mathrm{Re}^{0.687}\right),\ \frac{72}{\mathrm{Re}}\right],\ \frac{8}{3}\frac{\mathrm{Eo}}{\mathrm{Eo}+4}\right\} \tag{3}$$

At higher volume fractions of bubbles, the correction of Tsuji et al. [18] is applied:

$$C_D = C_{D0}\left(1 - \left(\frac{3\alpha_b}{\pi}\right)^{2/3}\right) \tag{4}$$

where α_b is the volume fraction of bubbles. This correction primarily accounts for acceleration of trailing bubbles. The drag force is proportional to the velocity difference between the gas bubbles and the surrounding liquid $\boldsymbol{u}_b - \boldsymbol{u}$. Note that $\boldsymbol{u}$ is the instantaneous velocity of the surrounding liquid

$$\boldsymbol{u} = \boldsymbol{U} + \boldsymbol{u}' \tag{5}$$

where $\boldsymbol{U}$ is the average velocity and $\boldsymbol{u}'$ is the turbulent fluctuations of the velocity. Thus, velocity fluctuations cause turbulent dispersion of bubbles through the drag force. Unless turbulence is fully resolved in the model, a sub-model is required to account for turbulent dispersion of the unresolved velocity fluctuations. For Lagrangian tracking of bubbles (or particles/parcels) we apply a *random walk model* [19] where the turbulent velocity fluctuations is calculated by

$$\boldsymbol{u}' = \boldsymbol{\xi}\sqrt{k_\Delta} \tag{6}$$

Here $\boldsymbol{\xi}$ is a Gaussian random number with zero mean and unit variance and k_Δ is the turbulent kinetic energy of the velocity spectrum not resolved by the model. The time for which this velocity fluctuation is applied in the integration of the bubble trajectory is limited by the eddy lifetime (or the time it takes for a bubble to traverse through a turbulent eddy). The eddy lifetime is [14]

$$\tau_e = \frac{3}{2}C_\mu \frac{k_\Delta}{\epsilon_\Delta} \cdot \mathrm{MIN}\left[1;\ \frac{\Delta\ \epsilon_\Delta}{k_\Delta^{3/2}}\right] \tag{7}$$

Virtual mass force also known as added mass force is the force perceived by the bubble since when it is accelerating it deflects and accelerates some of the surrounding water. The specific virtual mass force is given as

$$\boldsymbol{F}_{VM} = C_{VM}\frac{\rho}{\rho_b}\left(\frac{D\boldsymbol{u}}{Dt} - \frac{d\boldsymbol{u}_b}{dt}\right) \tag{8}$$

For the virtual mass coefficient $C_{VM} = 0.5$ is applied. Lift force is normally included in reactor modelling, but sensitivity studies show no effect of the lift force in typical bubble plumes in open waters. This is due to the absence of walls close to the bubbles. In such scenarios the shear rate is relatively small and the lift force can be discarded [12]. Bubble induced turbulence can be important close to the release point where the bubbly flow is dense. Since the flow is not sufficiently resolved in this region and the mechanism is not properly understood (see discussion by Olsen et al. [14] and Schwarz [20]), bubble induced turbulence is neglected. This can cause an uncertainty in the estimate of forces and spreading in the plume close to the release. Fortunately, this region is normally very small for most scenarios.

An estimate of the bubble size is required for calculating the drag coefficient (see Eq. (2)) and the mass transfer rate (see below). In dense and turbulent bubble plumes, the bubble size is governed by turbulent break up and coalescence. Mass transfer and gas expansion due to pressure gradients will dominate in dilute plumes. Laux and Johansen [21] developed a bubble size model for an Eulerian framework accounting for break up and coalescence. This can be recast into a Lagrangian framework. When also including the effect of mass transfer and gas expansion, the bubble size is expressed by the following differential equation

$$\dot{d}_b = \frac{d_b^{eq} - d_b}{\tau_{cb}} + \frac{d_b}{3}\left(\frac{\dot{m}_b}{m_b} - \frac{\dot{\rho}_b}{\rho_b}\right) \tag{9}$$

where m_b is the mass of a bubble, $\dot{m}_b$ is the mass transfer rate from a bubble, $\dot{\rho}_b$ is the Lagrangian time derivative of the bubble density, τ_{cb} is the time scale for coalescence or break up and d_b^{eq} is the bubble diameter obtained by a bubble if it is exposed to given flow conditions (turbulent dissipation and volume concentration) for a long time (i.e. equilibrium is reached). The equilibrium bubble diameter is

$$d_b^{eq} = C_1\sqrt{\alpha_b}\frac{\left(\sigma/\rho\right)^{0.6}}{\epsilon_\Delta^{0.4}}\left(\frac{\mu_b}{\mu}\right)^{0.25} + C_2 \tag{10}$$

where α_b is the volume fraction of bubbles, σ is the surface tension and ϵ_Δ is the sub grid turbulent energy dissipation. For the model coefficients we assume $C_1 = 4.0$ (typical for bubbles in liquids) and $C_2 = 200\ \mu$m (smallest expected bubble size). For further details, including time scale for coalescence or break up, refer to Laux and Johansen [21]. The initial bubble size for bubbles released from the release source is calculated by an empirical jet model [22]. As the bubbles change size, their mass also changes. Mass conservation is then assured by adjusting the number of bubbles in the parcel such that total mass of a parcel is unchanged during the process of coalescence and break up of bubbles.

The motion of the water (i.e. background fluid) is coupled to the bubble motion through drag forces and turbulence. Flow of seawater and the atmosphere above is calculated by the Navier–Stokes equations in an Eulerian frame of reference and utilizing a VOF method [23] which also tracks the interface between the continuous water and the atmosphere by the geometric-reconstruct scheme [24]. Mass conservation is ensured by the continuity equation:

$$\frac{\partial(1-\alpha_b)\rho}{\partial t} + \nabla\cdot(\rho(1-\alpha_b)\boldsymbol{v}) = S_b^c \tag{11}$$

where S_b^c is the source term to the continuity equation accounting for mass transfer with the Lagrangian bubble phase. We assume that the flow is dilute, and the effect of the bubbles can be neglected in the above equation. Thus we apply the following continuity equation:

$$\frac{\partial\rho}{\partial t} + \nabla\cdot(\rho\boldsymbol{v}) = S_b^c \tag{12}$$

Since motion in both water and atmosphere is accounted for, the continuous phase (i.e. background fluid) is described by mixture properties. Thus, the continuous phase density is

$$\rho = \alpha_w \rho_w + (1 - \alpha_w)\rho_a \tag{13}$$

where subindex w symbols water and subindex a symbols atmosphere. Viscosity and other properties are calculated equally. For conservation of momentum we follow the same procedure as for conservation of mass and assume dilute flow. The conservation equation then simplifies to the Reynolds averaged Navier–Stokes (RANS) equations for single phase flow

$$\rho \frac{D\mathbf{U}}{Dt} = \rho \boldsymbol{g} - \nabla p + \nabla \cdot \left[\mu_{\text{eff}}\left(\nabla \boldsymbol{U} + \nabla \boldsymbol{U}^T\right)\right] + \boldsymbol{S}_b \tag{14}$$

where μ_{eff} is the effective viscosity (molecular + turbulent). The source term in Eq. (14), $\boldsymbol{S}_b$, is the source term due to drag of bubbles

$$\boldsymbol{S}_b = \sum^{\frac{18\mu C_D \text{Re}}{24\rho_b d_b^2}} (\boldsymbol{u}_b - \boldsymbol{u})\zeta_b \frac{\Delta t}{\Delta V_c} \tag{15}$$

Here ζ_b is the mass flow rate of bubbles moving through the computational cell,[1] Δt is the time step and ΔV_c is the volume of the computational cell. This term provides a strong coupling to the Lagrangian bubble tracking. A similar coupling also appears for the virtual mass force. This is however almost insignificant and thus the expression is not listed here. These equations are based on the assumption that the flow is dilute (i.e. the volume fraction of the bubbles is small). This assumption is sometimes violated in the region close to the release source. As long as the region where the assumption is violated is small compared to the total domain, the overall results are not affected [25]. For scenarios with a greater extent of non-dilute conditions (i.e. shallow release with high release rate), a full two-way coupling [26] could be implemented.

Turbulence and turbulent viscosity μ_t is accounted for by a VLES model. Large scale turbulence is inherently captured by the momentum equations and only subgrid scale turbulence is modelled. Practically this is done by modifying the turbulent viscosity in the k-ϵ model, μ_t, by introducing a filter function [27]

$$\mu_t = C_\mu \ \rho \frac{k_\Delta^2}{\epsilon_\Delta} \ \cdot \text{MIN}\left[1;\ \frac{\Delta\ \epsilon_\Delta}{k_\Delta^{3/2}}\right] \tag{16}$$

Here Δ is a filter size (e.g. the mesh size can be used for filter size) which provides a length scale below which turbulence is not resolved. C_μ is a model coefficient. The unresolved turbulence (i.e. sub-grid turbulence) is calculated with the standard k-ϵ model [28]. Turbulent kinetic energy and turbulent dissipation is solved from

$$\frac{\partial}{\partial t}(\rho k_\Delta) + \nabla \cdot (\rho \boldsymbol{u} k_\Delta) = \nabla \cdot \left[\left(\mu + \frac{\mu_t}{\sigma_k}\right)\nabla k_\Delta\right] + G_k + G_b - \rho \epsilon_\Delta \tag{17}$$

$$\frac{\partial}{\partial t}(\rho \epsilon_\Delta) + \nabla \cdot (\rho \boldsymbol{u} \epsilon_\Delta) = \nabla \cdot \left[\left(\mu + \frac{\mu_t}{\sigma_\epsilon}\right)\nabla \epsilon_\Delta\right] + C_{1\epsilon}\frac{\epsilon_\Delta}{k_\Delta}(G_k + C_{3\epsilon}G_b) - C_{2\epsilon}\rho\frac{\epsilon_\Delta^2}{k_\Delta} + S_\epsilon \tag{18}$$

where G_k denotes generation of turbulent kinetic energy due to mean velocity gradients

$$G_k = \left[\mu_t\left(\nabla \boldsymbol{u} + \nabla \boldsymbol{u}^T\right) - \frac{2}{3}\boldsymbol{\delta}\rho k_\Delta\right] \cdot \nabla \boldsymbol{u} \tag{19}$$

G_b denotes generation of turbulence due to buoyancy

$$G_b = \tau_e \cdot \mu_t\left(\nabla \boldsymbol{u}_c + \nabla \boldsymbol{u}_c{}^T\right) \cdot \nabla \boldsymbol{g} + \rho\frac{2}{3}\tau_L \boldsymbol{g} \cdot \nabla \alpha \tag{20}$$

$C_\mu = 0.09$, $C_{1\varepsilon} = 1.44$, $C_{2\varepsilon} = 1.92$ and $C_{3\varepsilon} = 1.0$ are model coefficients calibrated against experimental data. The advantage of the VLES model compared to the k- ϵ model is that the large scale turbulence inherently calculated by the momentum equations does not rely on the model coefficients which is calibrated for steady state conditions at much smaller scales [29].

Turbulence is damped at the interface between the continuous liquid phase and the gas phase above because turbulent structures are not carried through the interface. This is not inherently accounted for by VOF models since the interfaces are not treated as boundaries. Thus a source term in the dissipation equation for turbulence is added to increase dissipation and dampen turbulence at the interface [30]. It is designed such that it forces the energy dissipation, ε, close to the surface to obtain a value equivalent to a turbulent length scale approaching zero at the surface. The target value of energy dissipation at the surface is given by

$$\epsilon_{new} = \frac{C_\mu^{3/4} k_\Delta^{3/2}}{\kappa l_s} \tag{21}$$

[1] The contribution of all parcels in the cell is added with adjustment for residence time in cell relative to time step. Volume fraction is calculated similarly.

l_s is the distance to the surface and $\kappa = 0.4$ is the von Karman constant. Numerically the energy dissipation is modified to approach this value by the following source term in the energy dissipation equation:

$$S_{sd} = N(\epsilon_{new} - \epsilon_{\Delta}) \tag{22}$$

Here S_{sd} is the source term due to surface damping and N is a large number. It needs to be sufficiently large to force ε_{Δ} to approach ε_{new}, but not too large which will cause numerical stability issues.

2.2. Mass transfer

Gas dissolution of gas species between bubbles and the surrounding ocean becomes significant if the bubbles reside sufficiently long in the ocean. Gas dissolution is a mass transfer process and the mass transfer rate for a single bubbles is

$$\dot{m}_i = A_b J_i = \pi d_b^2 k_i \cdot \left(c_i^{sol} - c_i^{\infty}\right) \tag{23}$$

where d_b is bubble diameter, k_i is mass transfer coefficient of species i, c_i^{sol} is solubility of species i and c_i^{∞} is the background concentration of species i in the surrounding water. The driving force is the difference in solubility and background concentration. It appears that mass transfer increases with increasing bubble size. This is true for single bubbles, but for a bubble plume the governing parameter is the mass transfer rate per mass of bubbles, i.e. the specific mass transfer rate

$$\frac{\dot{m}_i}{m_i} = \frac{A_b}{\rho_b V_i} J_i = \frac{6}{\rho_b d_b} k_i \cdot \left(c_i^{sol} - c_i^{\infty}\right) \tag{24}$$

The total interfacial area per mass or volume increases with decreasing bubble size. Thus, smaller bubbles give more mass transfer in total for the whole plume. The bubble size is estimated by Eq. (10). An important source of potential erroneous estimates of gas dissolution is the mass transfer coefficient k_i. The mass transfer coefficient varies significantly between clean and contaminated conditions. This depends on the type and concentration of surfactants in the ocean. Numerous types of surfactants exist in the ocean. They are mainly the products of biological processes involving phytoplankton [31] and include substances such as polysaccharides, lipids and more [32]. Thus, the amount of surfactants in the ocean varies with location, depth and season [33] as does the concentration of phytoplankton. Larger bubbles tend to refresh its boundary layer due to vortex shedding. This increases the driving force of the mass transfer and hence larger bubbles are more likely to act as bubbles in clean conditions. Although there are limited experiments on bubbles in seawater, it is believed that the mass transfer coefficient sees a shift to clean conditions when increasing in size between 3 and 4.5 mm [34].

Many correlations for the mass transfer coefficient exists for both clean and contaminated conditions [35]. Higbie [36] derived an expression for the mass transfer coefficient for clean conditions

$$k_i = \frac{2}{\sqrt{\pi}} \sqrt{\mathrm{Re}\ \mathrm{Sc_i}}\ \frac{D_i^w}{d_b} \tag{25}$$

where D_i^w is the diffusion coefficient of species i in sea water. The Schmidt number, $\mathrm{Sc}_{i,}$ describes the ratio between momentum and mass diffusion of species i in the surrounding water

$$\mathrm{Sc}_i = \frac{\mu}{\rho D_i^w} \tag{26}$$

Frössling [37] derived an expression for rigid spheres which represents a low value for mass transfer of bubbles in contaminated conditions

$$k_i = \left(2 + 0.6\ \mathrm{Re}^{1/2}\mathrm{Sc_i}^{1/3}\right)\ \frac{D_i^w}{d_b} \tag{27}$$

In order to acknowledge the observation that the bubble's shift their behavior from contaminated to clean behavior as the bubble size increases, a linear shift between the correlations of Higbie and Frössling is applied between 3.5 and 4.5 mm. This correlation describes the mass transfer coefficient for bubbles in seawater and is categorized as a correlation for partly contaminated conditions. The correlation is plotted in Fig. 1. More details on this is provided by Olsen et al. [34].

The above explains that estimates of gas dissolution are sensitive to the mechanisms governing the mass transfer coefficients. Eqs. (23) and (24) show that gas dissolution also depends on solubility, c_i^{sol}, and background concentration, c_i^w. Background concentration is inherently calculated by the model via a species conservation equation for the soluble gas components

$$\frac{\partial c_i^w}{\partial t} + \nabla \cdot \left(\boldsymbol{U} c_i^w\right) = D_i^w \nabla^2 c_i^w\ + S_b^{ci} \tag{28}$$

Here S_b^{ci} is the source term accounting for the amount of species i which is dissolved into water.

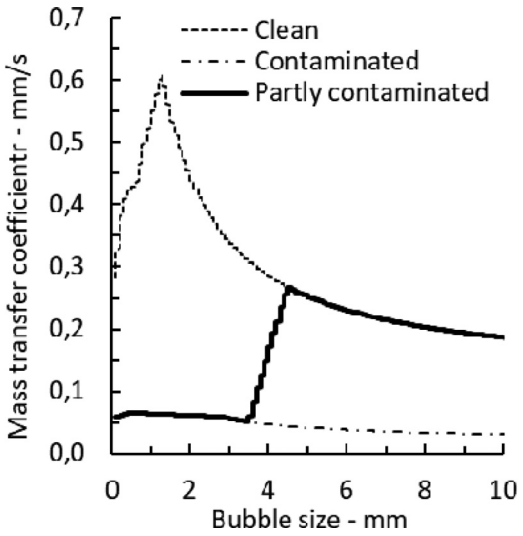

Fig. 1. Mass transfer coefficient as function of bubble size for clean [36], contaminated [37] and partly contaminated conditions [34].

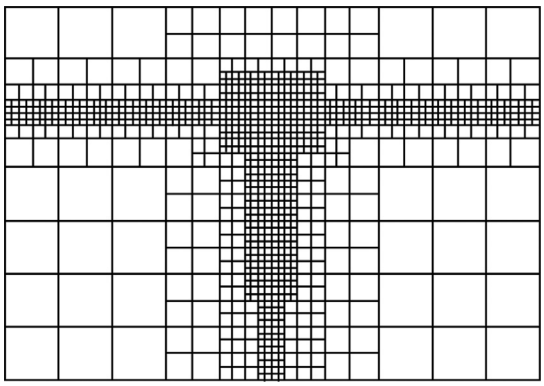

Fig. 2. Gridding concept with 3 levels of grid refinement.

2.3. Grid and numerical scheme

The above equations are solved in the commercial software ANSYS/Fluent 16.2 linked to a large set of developed code (user defined functions) for material properties, mass transfer, turbulence model (VLES) and more. The non-linear set of differential equations for the Eulerian phases is solved with the PISO scheme (pressure implicit with splitting of operator) for the pressure-velocity coupling and second order discretization for the conservation equations. Interface tracking and sharpening are performed by the geometric-reconstruct scheme [38]. Time step is adjusted to keep the Courant number below 0.25.

The computational mesh is based on a crude uniform mesh which is refined by the oct–three method around the plume and the ocean surface. This assures an affordable computational cost, which is still high compared to the traditional integral models. The mesh is typically constructed from a base mesh with 5 cells covering the ocean height. Up to 4 levels of refinement is applied to the region around the plume and the ocean surface. Due to the extent of the ocean surface, any further refinement around it is very costly. Further refinement is done below the ocean surface to assure a certain number of grid cells across the plume. The plume normally widens in a cone shape and thus the finest resolution is required in the lower region where the plume is narrow. This is also the region with the highest velocity and thus the constraint on the time step is given by the high velocity and smaller grid size in the region close to the release. The gridding concept is shown in Fig. 2.

A sensitivity study on grid refinement has been performed. In order to properly estimate the spreading of the plume it is important to resolve the governing physics as close to the release point as possible. By initiating the turbulent structures characteristic of the VLES-model as early as possible, good spreading predictions are obtained. With a coarse grid, turbulence will not be properly estimated, and turbulent dispersion will be underpredicted. Fig. 3 shows plume illustrations based on simulations with different grid refinement of a plume with a constant rate of 100 kg/s from 300 m depth. 6 levels are

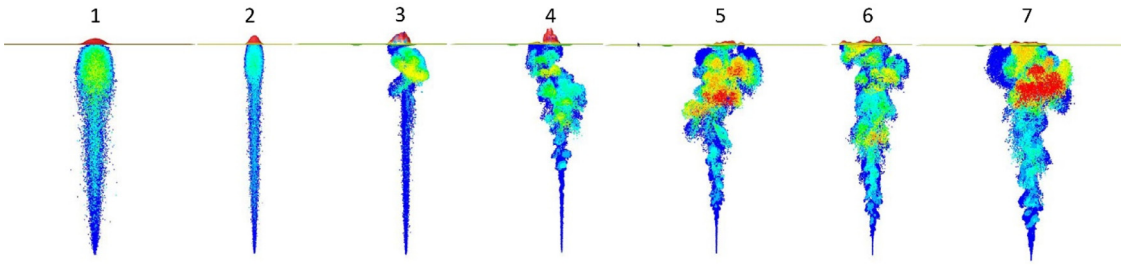

Fig. 3. Plume shapes with different levels of grid refinement. Low number is a coarse grid and high number a finer grid.

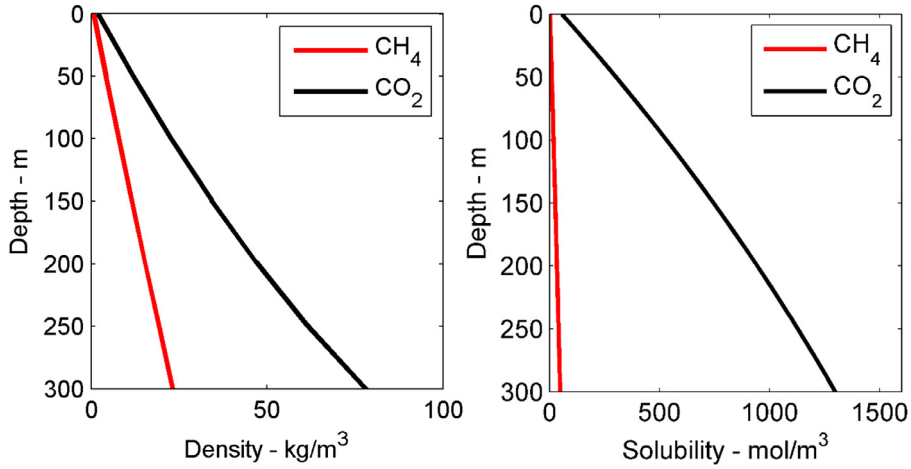

Fig. 4. Density and solubility of CH_4 and CO_2 as function of depth at 5 °C.

sometimes enough for shallower releases. 7 levels of refinement is sufficient for a wider range of depths. Grid independence up to 1000 m has been verified.

2.4. Material properties

The properties of gas depend on temperature and pressure and the properties of seawater itself is also a function of salinity. The density and viscosity of seawater is taken from Sharqawy et al. [39]. Different gas species have different properties. Two gases of concern are methane, CH_4, and carbon dioxide, CO_2. CO_2 is significantly heavier and more soluble than CH_4. This is seen in Fig. 4 where density and solubility are plotted. The properties found in NIST REFPROP [40] are applied. Diffusivity is important for mass transfer. CO_2 has roughly 2 times higher diffusivity than CH_4, which enhances mass transfer for CO_2 compared to CH_4. Quantitative numbers on diffusivity is found in [41] and typical values are 0.0011 mm^2/s for CO_2 and 0.0008 mm^2/s for CH_4 (taken at 5 °C).

3. Model validation

The model has been validated against a series of experiments and observations.

3.1. Rotvoll – release of air from 7 m

Engebretsen et al. [42] performed gas release experiments at Equinor's (formerly named Statoil) research facilities at Rotvoll in Trondheim. These experiments were used as the main validation set for the model in its early stage when the k-epsilon turbulence model was applied and gas dissolution could be neglected [11]. A series of releases were conducted in a rectangular basin with a depth of 7 m and a surface area of 6×9 m. The basin was filled with water and air was released at the bottom at gas rates of 83, 170 and 750 Nl/s (equivalent to 0.06, 0.12 and 0.54 kg/s referred to the state at the inlet). The inlet was comprised of a release valve with a rapidly acting piston injecting gas vertically with arrangements in front of it to reduce the vertical momentum. Because of this momentum breaker, the fluctuations in the gas flow and the length of the inlet jet were minimized.

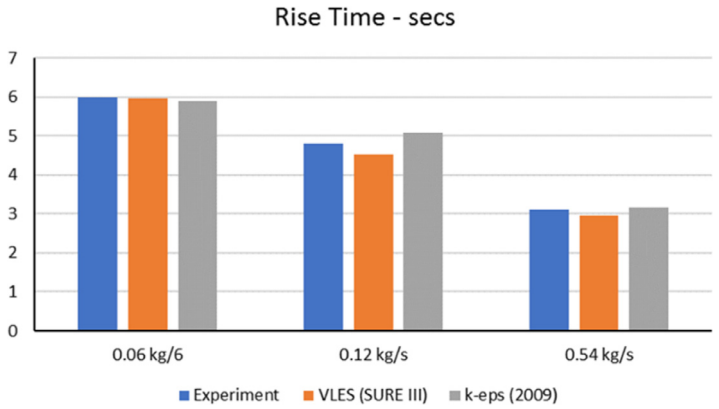

Fig. 5. Comparison of rise time observed in experiments and predicted by native model (k-eps) and enhanced model (SURE III).

Simulations with the latest version of the model including the VLES turbulence model described above was run with case definitions equivalent to those of the experiment at Rotvoll. We focused on the rise time of the first bubbles surfacing.[2] This is recorded from the simulation results and the experimental observations. Both the old version of the model with the k-epsilon turbulence model) and the new model are consistent with the experimental results as seen in Fig. 5 below.

Note that the rise time, or time of first penetrating gas, is defined as the first instance when a Lagrangian gas bubble is detected in a computational cell with a volume fraction of air (atmosphere) above 40%. This cell defines the water surface. The choice of 40% is to make sure that the bubbles don't leave the liquid phase prematurely, but results are not very sensitive to this choice.

3.2. Trolla – release of air from 30 m

An experiment part of the SURE project with release of air from 30 m depth outside Trondheim at a location known as Trolla was conducted by SINTEF [43]. The experiment was conducted from a barge with compressors delivering air through a hose to the specified depth. The arrangement caused a ramp up time of the release rate which was not insignificant. This needs to be accounted for when performing model simulations for comparison. In the experiments the rise time was based on three observation techniques; (1) an Echoscope imaged the rising plume by sonar signals, (2) wave guides monitored the rise of the ocean surface by conductivity measurements and (3) a camera was mounted at the top of crane looking down at the ocean surface. This provided three somewhat different definitions of surfacing of first gas.

The results are plotted in Fig. 6 for different release rates and for two different release diameters (1″ nozzle and 2″ nozzles were applied). Results from model simulations and observations show that the rise time decreases with increasing gas rate. This is as expected since increasing gas rates causes higher inlet velocities and a higher buoyant flux per volume. The model results do not match perfectly with any of the observational techniques, but the results are not dramatically off. These releases have a very high momentum and the resulting release jet penetrates quite far up in the water column. Such scenarios are among the most difficult to predict with the modelling concept. This is particularly difficult for the 1″ releases, since the release diameter is even less resolved. In most other cases the release jet only affects a very small part of the computational domain.

It should be noted that the 1″ releases take longer to surface than the 2″ releases. Due to larger resistance in the 1″ release nozzle, ramp-up time was twice that of the 2″ releases (7 versus 3.5 s for the three lower rates). This explains why the 1″ releases rise slower than the 2″ releases.

3.3. Buggs Springs – release of air from 50 m

Milgram [4] measured velocity profiles resulting from release of air in Bugg Springs (Florida) from a depth of 50 m for different release rates up to 0.71 kg/s. Simulations with the model were carried out with parameters and properties equivalent to those of the experimental values. The comparison between model and experiments is seen in Fig. 7. Here radial profiles of the vertical velocity at distances of 26 and 44 m above the release is plotted. Note that the experimental velocity profile is based on a velocity measurement averaged over 10 min and then curve-fitted to a Gaussian profile. The model results are averaged over 2 min after the plume has reached a quasi-steady state and thus the curves are not as smooth as the experimental curves. There is good consistency between experimental and calculated velocity profiles for most profiles. For the velocity profile 44 m above the release for the release rate of 0.34 kg/s there is, however, an overprediction of the

[2] The rise time is defined as the time between initial release of gas and surfacing of first gas

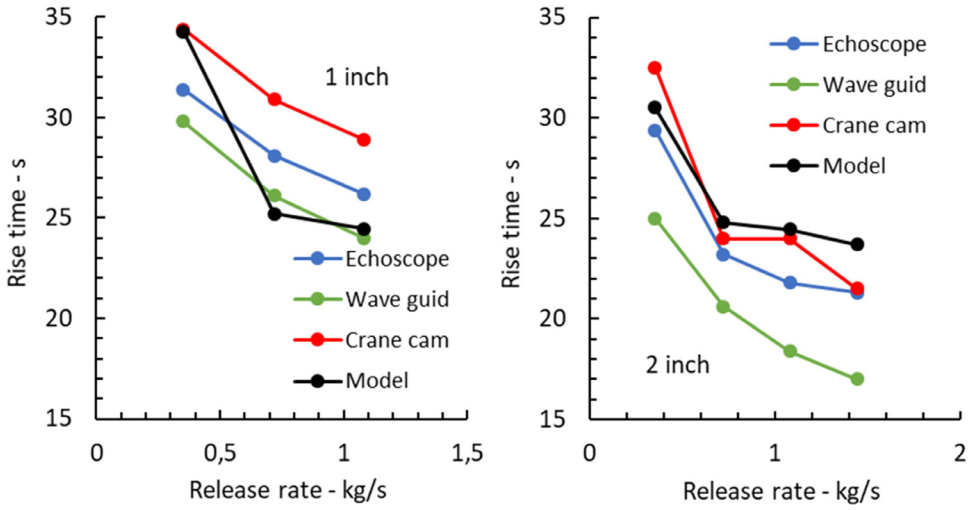

Fig. 6. Rise time as function of release rate estimated from different observational techniques and model simulations. Results from release with 1″ nozzle is seen to the left and 2″ nozzle to the right.

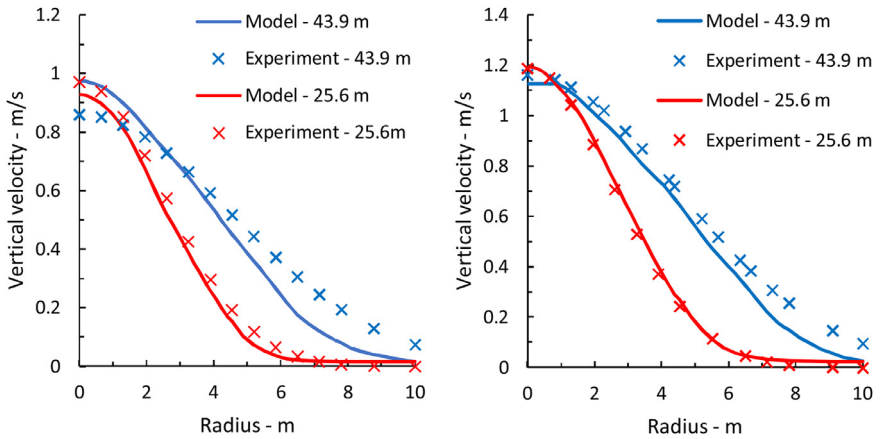

Fig. 7. Comparison of velocity profiles 26 and 44 m above release between model and experimental observations for release rate of 0.34 kg/s (left) and 0.71 kg/s (right).

peak velocity by 12% compared to the experiments. Reasons for this deviation has not been clarified. Other velocity profiles not shown here are more consistent.

A comparison between the VLES and k-epsilon turbulence model on prediction of plume angle is shown in Fig. 8. The VLES model is more consistent with the experimental observations than the k-epsilon model. The k-epsilon model predicts a plume angle almost independent of gas rate, whereas the VLES model and the observations show that the angle increases with gas rate up to a certain level.

3.4. Flags – release of natural gas from 138 m

During a pigging operation in the North Sea releases of natural gas was monitored by ocean sonar, aerial camera looking down at the ocean surface and other instruments [44]. Three releases from 138 m were studied and one from 380 m. The most intensive releases were two identical releases from 138 m with a release rate of approximately 17 kg/s which lasted for 120 s. The ascent of the plume front as function of time is seen in Fig. 9 where model prediction and observation of plume rise is shown. There is some signal noise in the observations of the early part of the release. Towards the end of the ascent the stochastic behavior of the turbulent eddy dominating the plume front is significant and can cause a deviation from the observation. The model predicts a rise time of 84 s, while 88 s was observed. The deviation is acceptable, especially when considering the stochastic input from the turbulence. The model prediction is consistent with the observations, but multiple simulations with a statistical treatment can improve the consistency further.

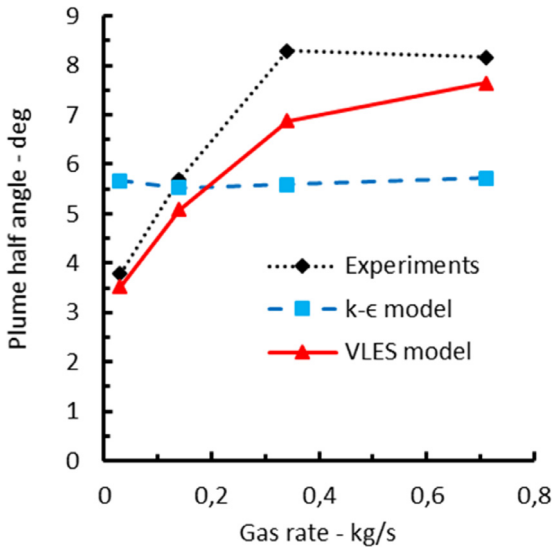

Fig. 8. Comparing plume spreading between Bugg Springs experiments and model predictions with VLES and k-epsilon turbulence models.

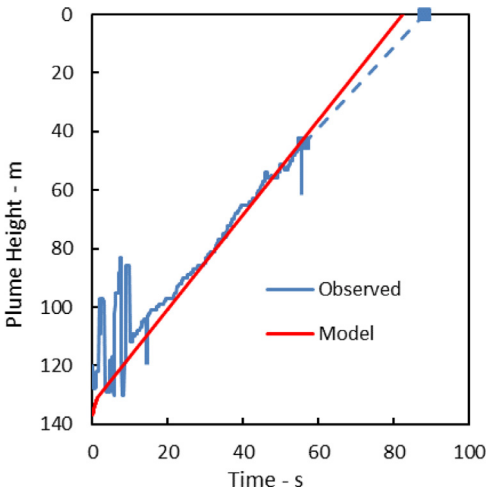

Fig. 9. Depth of plume front as function of time for 17 kg/s of natural gas from 138 m.

4. Case study on release of CO_2 vs CH_4

Release of natural gas and methane has been analyzed for decades due the safety aspects in offshore operations. Due to the recent interest in carbon storage and subsea transport lines for CO_2, safety assessments of CO_2 subsea release need more attention. As an attempt to bring some knowledge to this topic, simulations on CO_2 release and CH_4 release have been performed. The model presented above was applied in these simulations. It should be noted that the model has not been validated against plume data on CO_2 releases. It has been validated against plume observations on releases of air and natural gas. It is then assumed that the model is valid for other gases if proper material properties are applied. A comparison to the single bubble experiments on CO_2 [45] showed good consistency between model and observations. Similar justification was made by Dissanayake et al. [46] who studied CO_2 plumes with an integral model after validating the model against air and natural gas plume observations and CO_2 comparison only to single bubble experiments.

Since CO_2 is much more soluble in water than CH_4, scenarios with small gas rates has not been chosen since these are believed to fully dissolve in the ocean for the CO_2 releases. Releases from a depth of 100 m was studied first. The volumetric release rate was kept constant for both gases at 426 MMSCFD and 1277 MMSCFD. This is equivalent to 100 kg/s and 300 kg/s of CH_4 and 275 kg/s and 825 kg/s of CO_2. These are high release rates. The results are seen in Fig. 10. For the release of CH_4 of 426 MMSCFD about 25% of the gas is dissolved and for 1277 MMSCFD about 16% is dissolved. Hence, the majority of the released CH_4 reaches the atmosphere while the released CO_2 never reaches the atmosphere due to significantly higher gas dissolution.

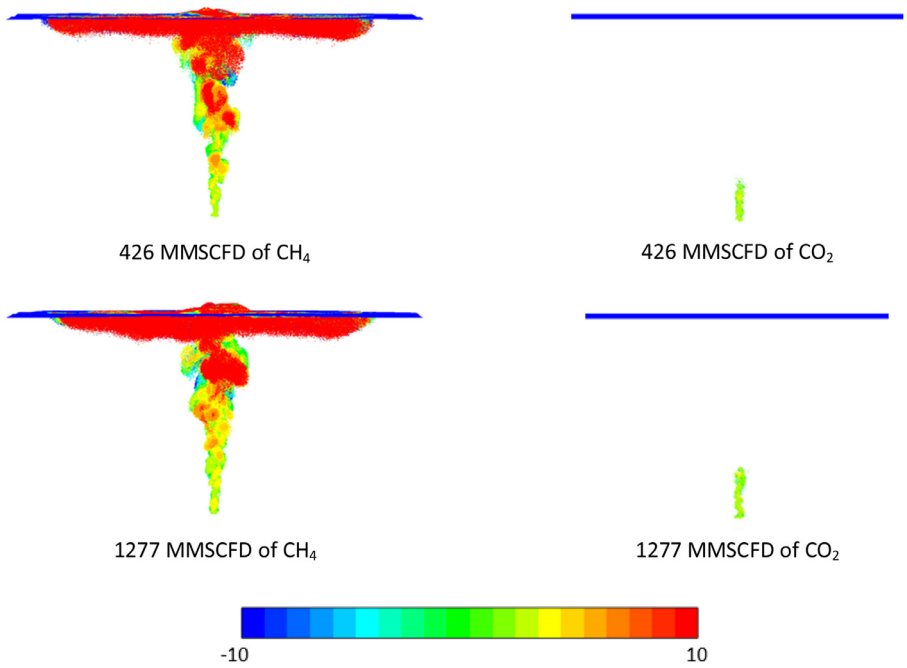

Fig. 10. Images of bubbles plumes from release of CH_4 and CO_2 from 100 m. Colors indicates distance from the plume axis towards the viewer (equivalent to an image by a sonar).

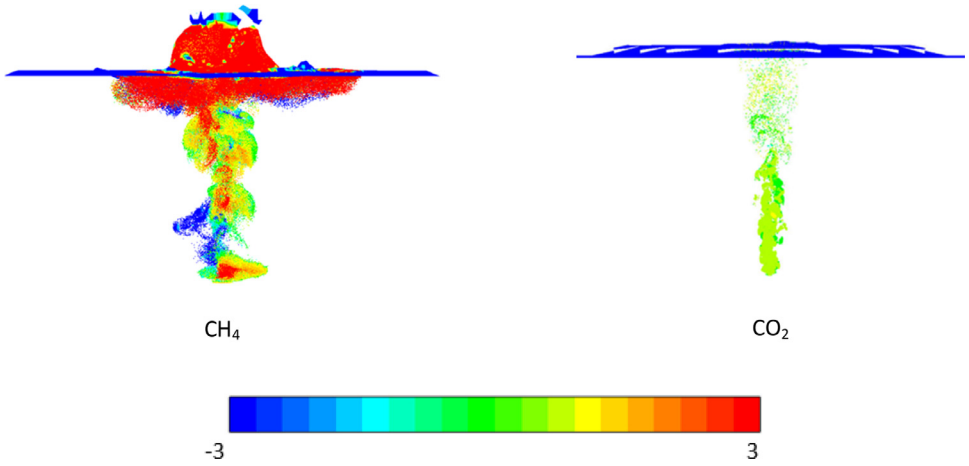

Fig. 11. Images of bubbles plumes from release of 426 MMSCFD of CH_4 and CO_2 from 100 m. Colors indicates distance from the plume axis towards the viewer (equivalent to an image by a sonar).

Secondly a release of 426 MMSCFD from 30 m was studied. The results are illustrated in Fig. 11. At this depth the gas reaches the surface faster and there is less time for gas dissolution. Still only about 1% of the released CO_2 reaches the surface and about 99% is dissolved. All of the CH_4 surfaces. Note that for CH4 this is an extreme blowout at which the resulting volume fractions of gas bubbles exceeds the model assumptions (typical for shallow release at very high gas rate). Thus, care must be taken in concluding too much from the CH_4 result for this scenario. Still it is clear that gas dissolution is practically insignificant for the CH_4 release. These results indicate that gas dissolution is a dominating mechanism in subsea gas release of CO_2 and the extent of this reduces the risk for surface operations. It should be noted that CO_2 dissolved in the ocean affects the pH level and thus the environmental impact may be far worse than the safety impact.

5. Conclusions

An Eulerian-Lagrangian mathematical modelling concept based on CFD for studying subsea gas releases has been derived and documented. Simulations with the model are consistent with 4 different experiments varying in depth from 7 to 138

m. Releases dominated by high jet momentum shows less consistency between model and observations. The model can be applied to estimate how gas surfaces into the atmosphere from a subsea source. This is vital input to risk assessments.

A comparison based on simulation results of CO_2- and CH_4-releases was performed. Due the high density and solubility of CO_2 compared to CH_4, a smaller fraction of released CO_2 will reach the atmosphere than CH_4. Even for very high release rates and from relative shallow releases, there is not much CO_2 reaching the atmosphere. This is encouraging from a safety aspect, but the CO_2 dissolved in the ocean affects the pH level and poses a threat to marine life.

Acknowledgements

The work has been supported by Total, Equinor, Wild Well Control and PSA Norway.

References

[1] J.E. Olsen, P. Skjetne, Current understanding of subsea gas release - a review, Can. J. Chem. Eng. 94 (2016) 209–219.
[2] T.K. Fanneløp, K. Sjøen, Hydrodynamics of underwater blowouts, Norweg. Marit. Res. 4 (1980) 17–33.
[3] O. Johansen, H. Rye, C. Cooper, DeepSpill - Field study of a simulated oil and gas blowout in deep water, Spill Sci. Technol. Bull. 8 (2003) 433–443.
[4] J.H. Milgram, Mean flow in round bubble plumes, J. Fluid Mech. 133 (1983) 345–376.
[5] B.R. Morton, G.I. Taylor, J.S. Turner, Turbulent gravitational convection from maintained and instantaneous sources, Proc. Roy. Soc. A 234 (1956) 171–178.
[6] L. Zheng, P.D. Yapa, Modeling gas dissolution in deepwater oil/gas spills, J. Marine Syst. 31 (2002) 299–309.
[7] M.P. Schwarz, W.J. Turner, Applicability of the standard k-ϵ turbulence model to gas-stirred baths, Appl. Math. Model. 12 (1988) 273–279.
[8] S.T. Johansen, F. Boysan, Fluid dynamics in bubble stirred ladles: Part II. mathematical modelling, Metallur. Trans. B 19B (1988) 756–764.
[9] C. Swan, A. Moros, The hydrodynamics of a subsea blowout, Appl. Ocean Res. 15 (1993) 269–280.
[10] G.C. Buscaglia, F.A. Bombardelli, M. García, Numerical modeling of large-scale bubble plumes accounting for mass transfer effects, Int. J. Multiph. Flow 28 (2002) 1763–1785.
[11] S. Cloete, J.E. Olsen, P. Skjetne, CFD modeling of plume and free surface behavior resulting from a sub-sea gas release, Appl. Ocean Res. 31 (2009) 220–225.
[12] J.E. Olsen, M. Popescu, On the effect of lift forces in bubble plumes, Progr. Comput. Fluid Dyn. 5 (2014).
[13] J.E. Olsen, P. Skjetne, Modelling of underwater bubble plumes and gas dissolution with an Eulerian-Lagrangian CFD model, Appl. Ocean Res. 59 (2016) 193–200.
[14] J.E. Olsen, P. Skjetne, S.T. Johansen, VLES turbulence model for an Eulerian–Lagrangian modelling concept for bubble plumes, Appl. Math. Model. 44 (2017) 61–71.
[15] B. Fraga, T. Stoesser, C.C.K. Lai, S.A. Socolofsky, A LES-based Eulerian–Lagrangian approach to predict the dynamics of bubble plumes, Ocean Modell. 97 (2016) 27–36.
[16] X. Li, G. Chen, F. Khan, Analysis of underwater gas release and dispersion behavior to assess subsea safety risk, J. Hazard. Mater. 367 (2019) 676–685.
[17] A. Tomiyama, I. Kataoka, I. Zun, T. Sakaguchi, Drag coeffcients of single bubbles under normal and micro gravity conditions, JSME Int. J. Ser. B 41 (1998) 472–479.
[18] Y. Tsuji, Y. Morikawa, K. Terashima, Fluid-dynamic interaction between two spheres, Int. J. Multiphase Flow 8 (1982) 71–82.
[19] A.D. Gosman, E. Ioannides, Aspects of computer simulation of liquid-fuelled combustors, J. Energy 7 (1983) 482–490.
[20] M.P. Schwarz, Bubble induced turbulence in two-fluid simulation if bubbly flow, in: Proceedings of the 26th International Symposium on Transport PhenomenaLeoben„ Austria, 2015.
[21] H. Laux, S.T. Johansen, A CFD analysis of the air entrainment rate due to a plunging steel jet combining mathematical models for dispersed and separated multiphase flows, in: Fluid Flow Phenomena in Metals Processing, Symposium, San Diego, CA, 1999, pp. 21–30.
[22] L. Zhao, M.C. Boufadel, S.A. Socolofsky, E. Adams, T. King, K. Lee, Evolution of droplets in subsea oil and gas blowouts: development and validation of the numerical model VDROP-J, Mar. Pollut. Bull. 83 (2014) 58–69.
[23] C.W. Hirt, B.D. Nichols, Volume of fluid (VOF) method for the dynamics of free boundaries, J. Comput. Phys. 39 (1981) 201–225.
[24] D.L. Youngs, Time-dependent multi-material flow with large fluid distortion, in: K.W. Morton, M.J. Banes (Eds.) Numerical Methods for Fluid Dynamics, Academic Press 1982.
[25] J.E. Olsen, S. Cloete, Eulerian-Lagrangian methods for modeling of gas stirred vessels with a dynamic free surface, in: Proceedings of the 7th International Conference on Multiphase Flow - ICMFTampa, Florida, 2010.
[26] D. Darmana, N.G. Deen, J.A.M. Kuipers, Parallelization of an Euler–Lagrange model using mixed domain decomposition and a mirror domain technique: application to dispersed gas-liquid two-phase flow, J. Comput. Phys. 220 (2006) 216–248.
[27] J.E. Olsen, P. Skjetne, S.T. Johansen, VLES Turbulence Model for an Eulerian-Lagrangian Modelling Concept for Bubble Plumes, CSIRO, 2015.
[28] B.E. Launder, D. Spalding, The numerical computation of turbulent flows, Comput. Methods Appl. Mech. Eng. 3 (1974) 269–289.
[29] S.T. Johansen, J. Wu, W. Shyy, Filter-based unsteady RANS computations, Heat Fluid Flow 25 (2004) 10–21.
[30] Q.Q. Pan, J.E. Olsen, S.T. Johansen, M. Reed, L. Sætran, CFD study of surface flow and gas dispersion from a subsea gas release, in: Proceedings of the ASME 33rd International Conference on Ocean, Offshore and Arctic EngineeringSan Francisco, 2014.
[31] B. Sabbaghzadeh, R.C. Upstill-Goddard, R. Beale, R. Pereira, P.D. Nightingale, The Atlantic Ocean surface microlayer from 50°N to 50°S is ubiquitously enriched in surfactants at wind speeds up to 13ms1, Geophys. Res. Lett. 44 (2017) 1–7.
[32] I. Leifer, R.K. Patro, The bubble mechanism for methane transport from the shallow sea bed to the surface: a review and sensitivity study, Cont. Shelf Res. 22 (2002) 2409–2428.
[33] J.D. Pakulski, R. Brenner, Abundance and distribution of carbohydrates in the ocean, Limnol. Oceanogr. 39 (1994) 930–940.
[34] J.E. Olsen, D. Krause, E.J. Davies, P. Skjetne, Observations of rising methane bubbles in Trondheim Fjord and its implications to gas dissolution, J. Geophys. Res. Oceans 124 (2019) 1399–1409.
[35] R. Clift, J.R. Grace, M.E. Weber, Bubbles, Drops, and Particles, Academic Press, New York; London, 1978.
[36] R. Higbie, The rate of absorption of a pure gas into a still liquid during short periods of exposure, Trans. A.I.Ch.E. 31 (1935) 365–389.
[37] N. Frössling, Über die Verdunstung falender Tropfen, Beitr. Geophys. 52 (1938) 170–216.
[38] ANSYS, Fluent theory guide, www.ansys.com, 2015.
[39] M.H. Sharqawy, J.H. Lienhard, S.M. Zubair, The thermophysical properties of seawater: a review of existing correlations and data, Desalinat. Water Treat 16 (2010) 354–380.
[40] E. Lemmon, M. Huber, M. McLinden, NIST Reference Fluid Thermodynamic and Transport Properties Database (REFPROP), 23, NIST Standard Reference Database, 2007.
[41] W. Hayduk, H. Laudie, Prediction of diffusion coefficients for nonelectrolytes in dilute aqueous solutions, AiChE J. 20 (1974) 611–615.
[42] T. Engebretsen, T. Northug, K. Sjøen, T.K. Fanneløp, Surface flow and gas dispersion from a subsea release of natural gas, in: Proceedings of the 7th International Offshore and Polar Engineering Conference, Honolulu, International Society of Offshore and Polar Engineers, 1997, pp. 566–573.
[43] P. Skjetne, J.E. Olsen, E.J. Davies, F. Leirvik, D. Krause, G. Eidnes, Comparison of Meso scale subsea gas release with multiphase Eulerian–Lagrangian CFD model, ESRELSlovenia (2017).

[44] E.J. Davies, P. Skjetne, D. Krause, B. Welde, D.R. de Miranda, Measurments of large-scale subsea gas plumes, J. Hydraul. Eng., To be submittedBull Trimest Plan Fam(2019).
[45] F. Takemura, A. Yabe, Rising speed and dissolution rate of a carbon dioxide bubble in slightly contaminated water, J. Fluid Mech. 378 (1999) 319–334.
[46] A. Dissanayake, J.A. DeGraff, P.D. Yapa, K. Nakata, Y. Ishihara, I. Yabe, Modeling the impact of CO_2 releases in Kagoshima Bay, Japan, Jo. Hydro-Environ. Res. 6 (2011) 195–208.